New Journal of Physics
The open access journal at the forefront of physics

PAPER • OPEN ACCESS

Dual stage approach to laser-driven helical coil proton acceleration

To cite this article: S Ferguson *et al* 2023 *New J. Phys.* **25** 013006

IOP Publishing New J. Phys. 25 (2023) 013006 https://doi.org/10.1088/1367-2630/acaf99

New Journal of Physics
The open access journal at the forefront of physics

Deutsche Physikalische Gesellschaft DPG
IOP Institute of Physics

Published in partnership with: Deutsche Physikalische Gesellschaft and the Institute of Physics

OPEN ACCESS

RECEIVED
6 July 2022

REVISED
9 December 2022

ACCEPTED FOR PUBLICATION
3 January 2023

PUBLISHED
12 January 2023

PAPER

Dual stage approach to laser-driven helical coil proton acceleration

S Ferguson[1], P Martin[1], H Ahmed[1,2], E Aktan[3], M Alanazi[1], M Cerchez[3], D Doria[1,4], J S Green[2], B Greenwood[1], B Odlozilik[1], O Willi[3], M Borghesi[1] and S Kar[1,*]

[1] Centre for Plasma Physics, School of Mathematics and Physics, Queen's University Belfast, Belfast BT7 1NN, United Kingdom
[2] Central Laser Facility, Rutherford Appleton Laboratory, Didcot, Oxfordshire OX11 0QX, United Kingdom
[3] Institute for Laser and Plasma Physics, Heinrich Heine University of Düsseldorf, Düsseldorf D-40225, Germany
[4] Extreme Light Infrastructure (ELI-NP), and Horia Hulubei National Institute for R&D in Physics and Nuclear Engineering (IFIN-HH), Str. Reatorului No. 30, 077125 Bucharest-Magurele, Romania
[*] Author to whom any correspondence should be addressed.

E-mail: s.kar@qub.ac.uk

Keywords: proton acceleration, helical coil accelerators, laser driven ion acceleration

Abstract

Helical coil accelerators are a recent development in laser-driven ion production, acting on the intrinsically wide divergence and broadband energy spectrum of laser-accelerated protons to deliver ultra-low divergence and quasi-monoenergetic beams. The modularity of helical coil accelerators also provides the attractive prospective of multi-staging. Here we show, on a proof-of-principle basis, a two-stage configuration which allows optical tuning of the energy of the selected proton beamlet. Experimental data, corroborated by particle tracing simulations, highlights the importance of controlling precisely the beam injection. Efficient post-acceleration of the protons with an energy gain up to ∼16 MeV (∼8 MeV per stage, at an average rate of ∼1 GeV m^{-1}) was achieved at an optimal time delay, which allows synchronisation of the selected protons with the accelerating longitudinal electric fields to be maintained through both stages.

1. Introduction

Proton acceleration using high power laser drivers has shown progress at a significant pace over the past two decades, motivated by the vision of delivering a compact and cost-effective alternative to conventional accelerators. Laser-driven sources, moreover, possess a unique ultra-short burst duration, enabling beam delivery at exceptionally high currents and dose rates [1]. In this context, target normal sheath acceleration [2] (TNSA) has been the most widely studied mechanism of ion acceleration from an intense laser pulse, where ions are accelerated by the space charge field set up by a hot electron sheath at the rear side of foil targets irradiated by intense lasers. This mechanism produces a proton burst that has a relatively wide angular spread (∼10°–20° half-angle), with a broadband, exponentially decaying spectrum, thus limiting the proton flux at high energies. The development of helical coil (HC) accelerators, as first proposed in [3, 4], has therefore shown promise to mitigate these inherent disadvantages of the TNSA mechanism, and potential as a laser driven alternative to conventional radio frequency (RF) accelerators for medical applications [5–8], production of secondary radiation sources [9–11], and high energy density physics [12]. The energy selection characteristic of the HC scheme is advantageous for the aforementioned applications, as, for instance, accurate control of the proton bunch energy is essential for applying Bragg peak penetration for targeted hadron therapy. Furthermore, high brilliance beams are also highly desirable for these applications, and the HC scheme delivers the large particle flux of TNSA at the desired proton bunch energy by chromatic focusing.

The HC accelerators [3, 4, 13, 14] consist of a helix of wire perpendicular to the rear surface of a typical flat foil (FF) target. Irradiating the foil generates simultaneously a proton beam at its rear surface and a positively charged unipolar electromagnetic (EM) pulse, tens of ps in duration, which flows along the helix wire at $v_{EM} \simeq 0.98c$ [3, 15–17]. The travelling EM pulse along the helical path produces a strong EM field

region within the HC, with strong radial and longitudinal components, the former of which acts to focus and collimate protons directed along the helix axis, while the latter accelerates them further, resulting in a quasi-monoenergetic, highly collimated proton bunch emerging from the end of the HC. The specific proton energy which is synchronised with the velocity of the EM pulse along the helix axis can be selected by careful control of the HC diameter and pitch. Pencil beams of energies of up to 50 MeV have recently been demonstrated using a single HC at a petawatt-class laser facility [13].

While the beam energies can be further improved by optimising the HC design and using ultra-high intensity laser drivers, the same outcome can be achieved by multi-staging HCs while using multiple high intensity laser pulses. A proof-of-principle demonstration of multi-staging HC modules is reported in this article, where the proton bunch generated from one HC is further accelerated in a second HC driven by a separate laser. Under optimum injection conditions, the resulting energy gain of the proton bunch was double that of a single stage. This method also addresses the issue of the accelerated proton bunch outrunning the electric field in a HC [18], which limits energy gain to the initial ∼10 mm of HC [13, 18]. A systematic temporal scan demonstrates that the spectral peak energy in a dual stage HC configuration is highly sensitive (on the ps scale) to the delay between the driving laser pulses, which is further corroborated by particle tracing simulations elucidating the injection dynamics of a TNSA seed beam of broad spectral profile.

2. Experiment

The experiment was performed using the Vulcan laser at the Rutherford Appleton Laboratory in the UK [19, 20]. A dual laser configuration was employed to drive the first and second stage HCs with separate irradiations as shown in figure 1. The first stage was driven by a (2.5 ± 0.3) ps pulse containing ∼50 J (henceforth CPA1) and the second stage by a (3.4 ± 0.9) ps pulse containing ∼60 J (henceforth CPA2), where laser energy is quoted post-compressor. Both beams were focussed after wavefront corrections, by $f/3$ off-axis parabolic mirrors to ∼5 μm full-width at half-maximum (FWHM) spots on target, each containing 35% of the delivered energy within the FWHM. This resulted in both beams delivering peak intensities of $\sim 3 \times 10^{19}$ W cm^{-2}. The first stage HC (henceforth called HC1) had an inner diameter $d_1 = 700$ μm and pitch $p_1 = 500$ μm, while the second stage HC (henceforth called HC2) had a smaller inner diameter $d_2 = 500$ μm and pitch $p_2 = 425$ μm. The increased pitch to diameter ratio of HC2 was chosen to synchronise higher energy protons with the objective of accelerating further the protons accelerated by HC1. Both HCs were constructed from stainless steel wire of diameter $d_w = 125$ μm and were 8.0 ± 0.3 mm long, separated by 3.5 ± 0.6 mm to minimise the influence of the EM pulse in one HC on the other. The lasers irradiated 2×2 mm FFs of 25 μm thick Au. The Au foil in the first stage (henceforth called FF1) was directly attached to HC1, seeding a proton beam within the HC. The second stage Au foil (henceforth called FF2) was attached to HC2 via a 125 μm diameter stainless steel connecting wire, manufactured to the specification shown in figure 1. This arrangement allowed the protons emitted from HC1 to be injected directly into HC2, avoiding any disruption due to the laser interaction with FF2, as well as the possibility of on-shot self-proton probing of the HC2 charge pulse interaction with the proton beam generated from FF2. In addition to the dual stage helical coil (DSHC) configuration shown in figure 1, several shots were taken in a single stage helical coil (SSHC) configuration were HC2 was removed and only CPA1 employed. The proton beams emitted from HCs were observed on stacks of radiochromic film (RCF) [21–24] at 75 mm from the proton source, as shown in figure 1.

The delay, τ, between the peak of the EM pulses entering HC1 and HC2, was controlled by varying the arrival of the laser pulses at their respective targets using optical delay lines built into the laser system. The delay incorporates the time taken for the EM pulse to flow from FF2 to HC2 along the connecting wire, which was calculated assuming a nominal speed of the EM pulse $v_{EM} \simeq 0.98c$, as measured in [3, 15–17] and the wire length measured from the photographs of the target taken before irradiation. The uncertainty in the calculation of τ is mainly a combination of the error in measuring the length of the connecting wire ($\pm$0.5 mm) and the error in synchronising CPA1 and CPA2 ($\pm$4 ps) using a fast photodiode connected to an oscilloscope.

3. Results

A selection of SSHC produced proton beams observed on RCF are shown in figure 2(a). As expected, the SSHC produced an ultra-low divergence proton beam (0.5° HWHM) at ∼24 MeV, with the beam divergence increasing to HC1's 2.5° half-angle aperture at lower and higher energies (figure 2(a)). The energy band of the collimated part of the beam represents the protons which have remained synchronised with the electric field throughout the HC and therefore have received maximum energy gain. As shown in figure 2(d) the

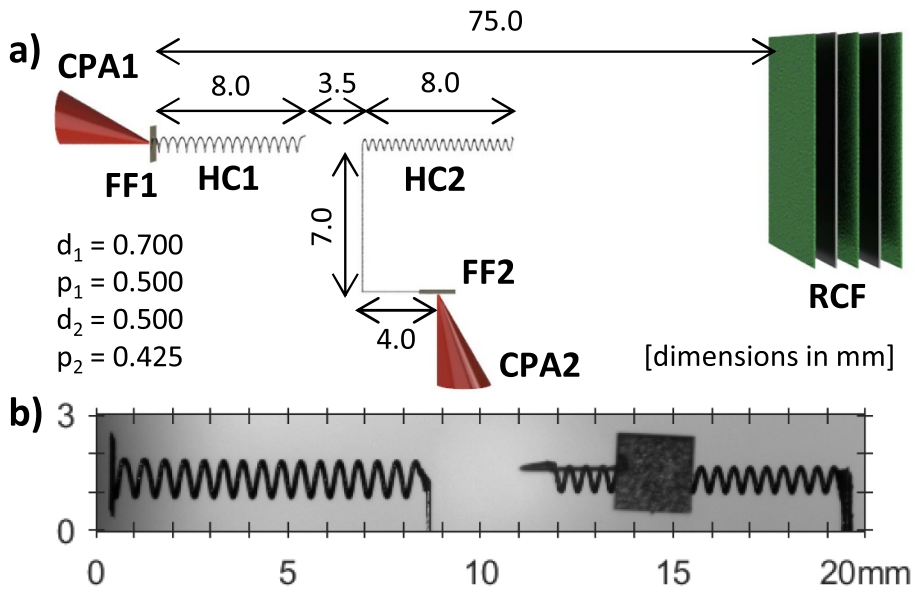

Figure 1. (a) Top view schematic of the experimental setup used for the dual stage helical coil (DSHC) (FF1/FF2 represent the flat foils on the first and second stages; HC1/HC2 represent the helical coils of each respective stage; and CPA1/CPA2 represent the laser pulses irradiating FF1/FF2 respectively. The parameters $(d_1, p_1)/(d_2, p_2)$ listed to the left represent the internal diameters, and the pitches of the HC1/HC2. and (b) a photograph (side view) of an experimentally deployed DSHC target.

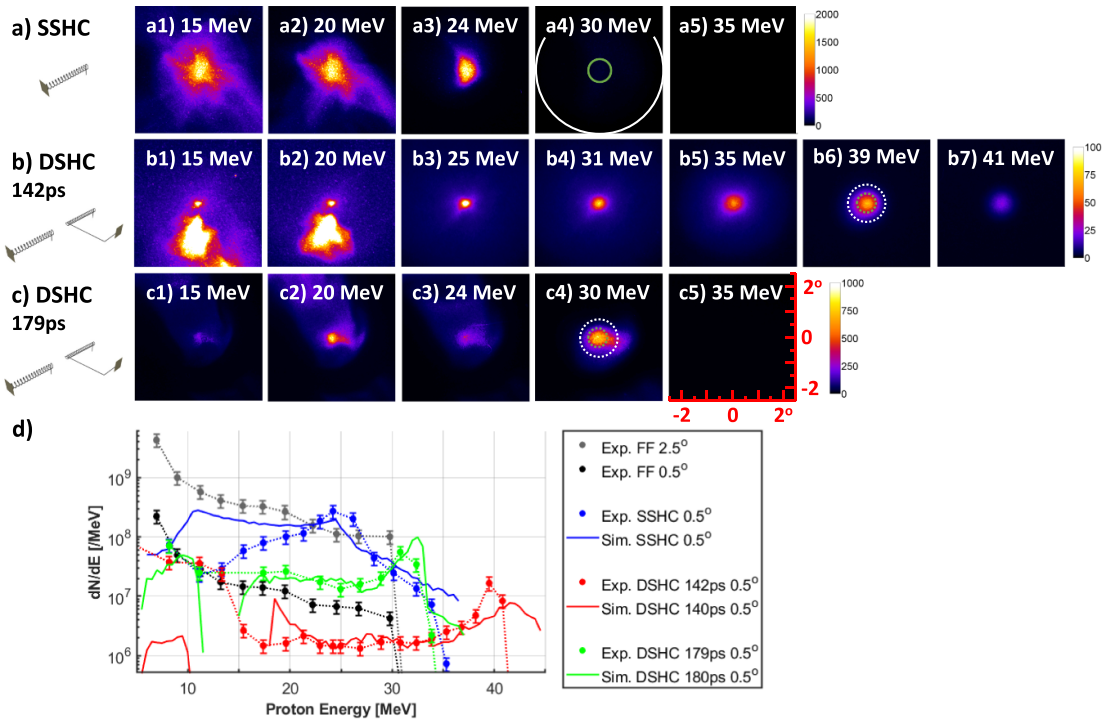

Figure 2. Proton beams observed on RCF from (a) a single stage helical coil (SSHC), (b) a dual stage helical coil (DSHC) with $\tau \simeq$ 142 ps and (c) a DSHC with $\tau \simeq$ 179 ps. Note lower sensitivity HD-V2 type RCF is shown in (a1-5) and (c1-3) while higher sensitivity EBT-3 type RCF is shown in (b1-5) and (c4-5). White solid (dotted) circles represent the 2.5° (0.7°) half-angle cone of the SSHC (DSHC) apertures. The green (red) circles encompass 0.45° (0.37°) half-angle cones for SSHC (DSHC) targets as the divergence is calculated from the HC exit opposed to the divergence scale which is calculated from the proton source at FF1. (d) Energy spectra extracted from dose converted RCF for a 0.5° half-angle cone from the HC exit (red solid and dotted circles) in (a)–(c) are shown in comparison to a typical proton spectra obtained from a flat foil (FF) for the same angular cone. A 0.5° half-angle cone was chosen as this is approximately the half-width at half-maxima (HWHM) of the most tightly focussed proton beams in HC shots, as seen in (a3), (b5) and (c4). A FF spectrum for a 2.5° half-angle cone is also shown for comparison. Spectra obtained from *PTRACE* simulations are over-plotted as solid lines.

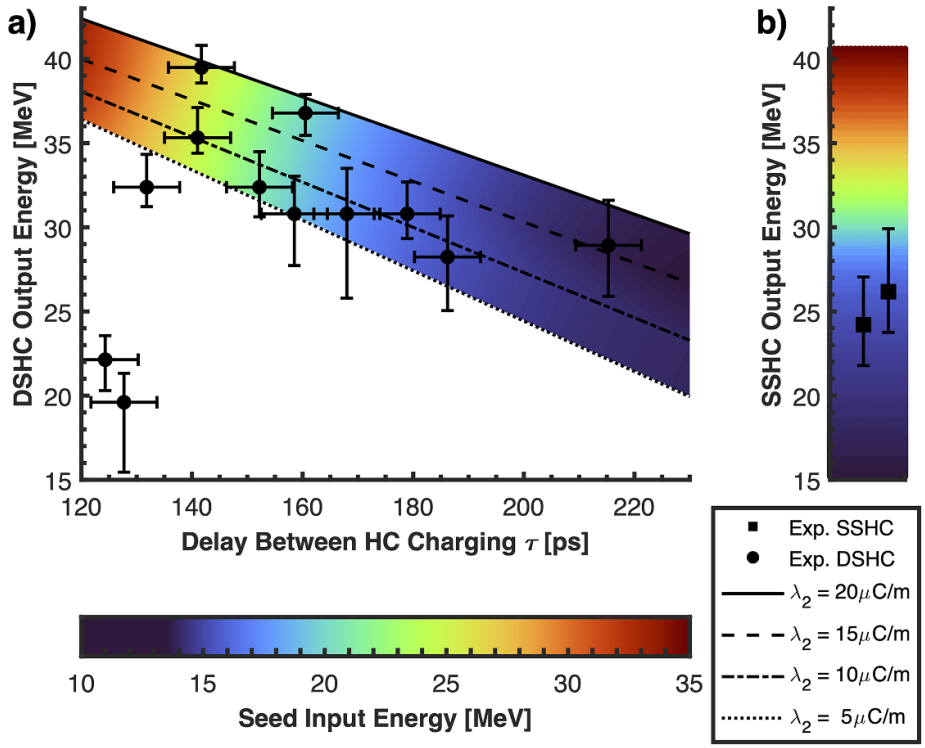

Figure 3. (a) Spectral peak energy obtained from a temporal delay scan in the experiment is shown, plotted over results obtained from *PTRACE* simulations. The simulated data is plotted as a colour mapped region, where the colour corresponds to the seed energy input into the first stage, as per the colourbar beneath the plot. The black lines represent the linear fit for the simulations with $\lambda_1 = 23\ \mu\text{C m}^{-1}$ and $\lambda_2 = 5$, 10, 15, & 20 $\mu\text{C m}^{-1}$. (b) SSHC data from the experiment plotted over simulation results showing the expected output energy from the first stage for different input energies. Vertical uncertainty bars represent the FWHM of the spectral peaks and horizontal bars represent the uncertainty in the measurement of τ.

SSHC spectrum exhibits a peak at ∼24 MeV corresponding to the optimal focussing seen on RCF. The SSHC provides a significant enhancement in proton flux, compared to the reference FF shot, over a broad energy range of 20–30 MeV due to the focussing, and post-acceleration of lower-energy, higher flux TNSA protons. The observed broad spectral profile of the HC-driven proton bunch is typical of the case where the HC is attached directly to the proton generating foil and the electric field pattern acts on a broadband proton energy range close to their source before they are significantly dispersed along the HC axis [3, 18, 25]. Such a broad spectral peak with moderately good collimation was chosen as a suitable candidate to study beam injection into a second stage, as discussed later, for the intended temporal scan covering a range of proton energies.

A systematic scan of the DSHC configuration was followed by varying the time at which protons from HC1 were injected into HC2. Figures 2(b) and (c) show a selection of RCF data obtained from two DSHC shots taken for $\tau \simeq 142$ ps and $\tau \simeq 179$ ps. As shown in figure 2(d), the proton spectra from the DSHC targets exhibit narrow-band spectral peaks at the maximally collimated energies. Although the second HC reaccelerates a part of the spectral peak delivered by the first stage, the number of particles delivered by the DSHC case within the spectral peak are significantly higher than that from the FF and the SSHC targets at similar energies. For example, 10^7 protons in the energy range 39–41 MeV would result in a dose deposited in water of 5 Gy, assuming a pencil beam width of 1 mm, which is high enough for therapeutic applications. Unlike the broad spectral peak obtained from the SSHC with coils attached to the FF, the spectral peaks from the DSHCs were significantly narrower, most likely as a result of the smaller bandwidth able to be selected by the HC2 due to temporal and spatial dispersion of protons along the HC axis during their time of flight across the length of HC1. Spectral bunches with a narrower bandwidth have also been observed in HC targets when including a delay line between the foil and the coil entrance [13]. The gap between the FF and the coil allows spatial dispersion of the TNSA protons, resulting in the charge pulse synchronising with a narrower energy range, similar to what occurs in the DSHC.

As expected, τ plays a crucial role in the DSHC configuration, controlling the spectral window selected by the HC2. Figure 3 shows the systematic temporal scan over ∼100 ps range as carried out in the experiment to study the dynamics of beam injection in DSHCs. Spectral peaks (with ultra-low divergence) are produced at higher energies by reducing τ, i.e. when higher energy protons from HC1 are injected into HC2 synchronously with the EM pulse. For instance, $\tau = 142$ ps and 179 ps, for the cases shown in figures 2(b) and (c), represent, as discussed later with the help of particle tracing simulations, timely injection of

∼26 MeV and ∼16 MeV protons from the FF1 in the HC2. The spectral peaks at ∼40 and ∼32 MeV observed for the two cases represent a significant (∼14 MeV and ∼16 MeV respectively) net gain in proton energy due to the DSHC configuration. The rapid drop in energy observed for shorter delays ($\tau < 140$ ps) is due to the lack of protons beyond 40 MeV produced by the first stage. In this scenario protons are injected into HC2 after the arrival of the peak of the EM pulse and experience a decelerating electric field.

4. Discussion

To interpret more accurately the experimental observations, the experiment was modelled in the particle tracing code *PTRACE* [26]. The input proton beam in the simulations was given a small 2.5° divergence cone and a Boltzmann-like TNSA spectral distribution with a 10 MeV temperature in the 10–30 MeV region of interest, as produced in experimental FF shots (figure 2(d)). The EM pulses produced at both stages were measured during the experiment employing the self-probing technique [17], where the proton beam produced by the interaction is deployed to probe the EM pulse generated from the same laser interaction. Firstly, the EM pulses produced by CPA1 and CPA2 were diagnosed independently by using an FF attached to a wire, arranged in a square wave pattern (SWP) facing the foil's rear side and in the line of sight of the TNSA protons. Proton deflection by the EM pulse propagating along the SWP wires led to depleted regions of dose surrounding the wire shadow on the RCF. The magnitude of the EM pulse travelling along a wire can typically be represented in terms of a linear charge density, which allows for numerical modelling of the EM pulse's radial electric fields in the simulations. By comparing the deflection of the protons at a given point on a given RCF layer to that caused by a charged wire modelled in PTRACE, one can reconstruct the linear charge density associated with the EM pulse at that point. Repeating this process for different points on each RCF layer, the velocity and temporal profile of the EM pulse along the SWP wire can be obtained [17]. The velocity of the EM pulse flowing along the wire was measured as $v_{EM} \simeq 0.98c$, in agreement with earlier works. The EM pulse temporal profiles were found as asymmetric Gaussians with $t_r \simeq 5$ ps half width at half maximum (HWHM) rise for both stages and $t_d \simeq 20$ ps (30 ps) HWHM decay time for first (second) stages. The measured rise and decay times are broadly in line with those measured previously at other laser systems [3, 4, 13]. Although a
detailed study of the EM pulse profile was not feasible during the campaign, the longer decay times measured in the current experiment may be attributed to the longer pulse durations of the interaction laser pulses. The interaction of CPA1 with the first stage produced a peak linear charge density measured as $\lambda_1 \simeq 23 \pm 3\ \mu\text{C m}^{-1}$. Although the SWP setup showed similar peak linear charge density for CPA2 as CPA1, on-shot self-proton probing of HC2 in a few shots indicated this stage's peak linear charge density to fluctuate in the range of $\lambda_2 \simeq (10 \pm 3) - (15 \pm 3)\ \mu\text{C m}^{-1}$. Since the CPA2 energy remained relatively stable between shots, the fluctuation in λ_2 may be arising from factors such as shot to shot variations in CPA2 pulse duration and alignment of the CPA2 on FF2, or suboptimal coupling of EM pulse to the coil in HC2 due to its complex geometry and fabrication.

A SSHC simulation with $\lambda_1 = 23\ \mu\text{C m}^{-1}$ produced a similar spectral profile as the experimental data, as shown in figure 2(d), for the focussed part of the beam. The residual discrepancy at lower energies arises due to highly non-uniform and diffused profile of the beam obtained in the experiment, most likely due to non-uniformity in the input beam profile not being focused effectively by the tailing part of the electric field region within the HC. Subsequently a series of DSHC simulations were performed in the parameter space of $\tau = 120 - 230$ ps and $\lambda_2 = 5 - 20\ \mu\text{C m}^{-1}$ with a fixed $\lambda_1 = 23\ \mu\text{C m}^{-1}$. As shown in figure 2(d), simulated spectra obtained for $\tau = 140$ ps with $\lambda_2 \simeq 20\ \mu\text{C m}^{-1}$ and $\tau = 180$ ps with $\lambda_2 \simeq 10\ \mu\text{C m}^{-1}$ are in good agreement with the experimental spectra obtained from their respective shots. The simulated peak energy for the full parameter space is plotted in figure 3(a) incorporating a colour scale representing the input energy (energy at FF1) corresponding to the spectral peak. As can be seen, the simulation indicates the synchronization of higher energy protons for lower τ, and the required proton energy beyond 35 MeV to achieve a net gain for $\tau < 140$ ps.

Figures 4(a) and (b) give a detailed account of the proton dynamics in the DSHC based on the $\tau = 140$ ps and $\tau = 180$ ps simulations, while using the same value of $\lambda_2 \simeq 20\ \mu\text{C m}^{-1}$ for a one-to-one comparison. Other simulation parameters were kept the same as those shown in figure 1(d). As can be seen in figures 4(a) and (b), HC1 in both cases accelerates seed protons above 14 MeV propagating within the positive longitudinal electric field region, while the <14 MeV seed protons propagating within the negative field region are decelerated. From figure 4(c) it can be seen that 15–16 MeV seed protons experience optimal focussing and acceleration in the HC1, which leads to the spectral peak observed at ∼24 MeV for the SSHC shown in figure 2(d).

Comparing figures 4(a1) and (b1) we see that altering τ translates the second stage electric field along the time axis, effectively synchronising the HC2 with a different energy band of the proton beam emerging from

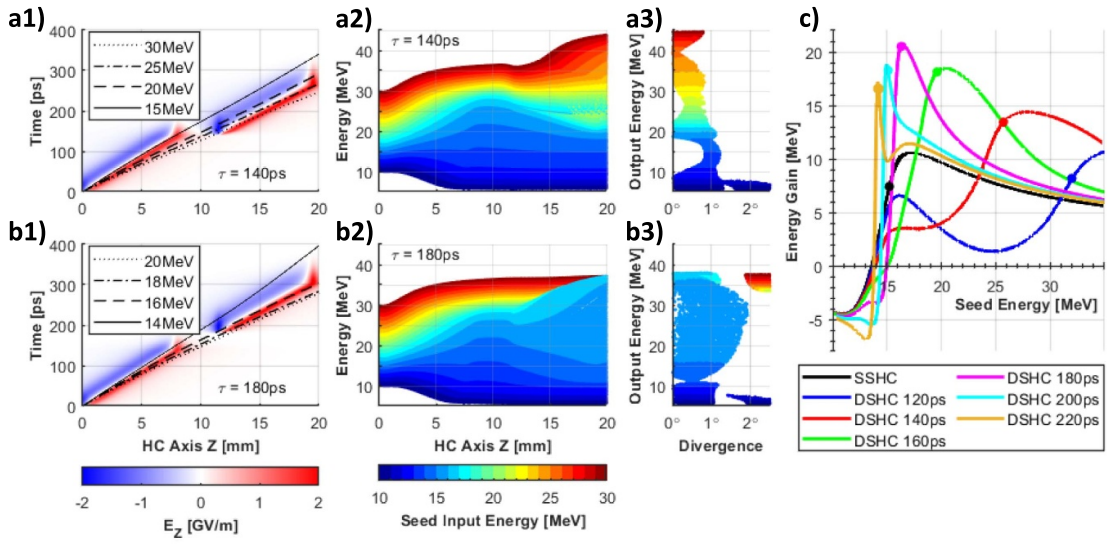

Figure 4. (a1) Proton time of flight along the HC axis with respect to the longitudinal electric field for a DSHC with $\tau = 140$ ps. The trajectories of several proton energies of interest, as obtained from *PTRACE* simulations, are shown with a key indicating their initial seed energy. (a2) The corresponding energy change as protons propagate through the DSHC and (a3) the beam divergence at the exit of the DSHC. (b) shows the same as (a) for a DSHC simulation with $\tau = 180$ ps. For reference, HC1 extends from 0.0 to 8.0 mm along the axis while HC2 extends from 11.5 to 19.5 mm. (c) Energy gain in a SSHC, and DSHCs with different delays. Dots indicate the positions in the graphs corresponding to maximum proton beam focussing. Here $\lambda_1 = 23\ \mu\text{C m}^{-1}$ and $\lambda_2 = 20\ \mu\text{C m}^{-1}$ are used in all simulations for ease of comparison between the different τ cases.

HC1. For $\tau = 180$ ps the accelerating electric field of HC2 synchronises with >15 MeV seed protons that have efficiently accelerated in the first stage. In particular, the ∼16 MeV seed protons receive near-maximum energy gain in both stages, leading to a highly efficient double-stage acceleration as shown in figure 4(c). Comparing this with the experimental data taken at $\tau = 180$ ps, as shown in figure 2(d), a net energy gain of ∼16 MeV (∼8 MeV per stage) is estimated to be produced in the DSHC target. On the other hand, in the $\tau = 140$ ps case the electric field at HC2 is formed significantly sooner than the arrival of the ∼ 16 MeV seed protons which are optimally accelerated by the HC1. Therefore, HC2 accelerates the highest energy protons produced by the HC1, although these emerge less collimated from the HC1 (figure 2(a)). The maximum energy gain in this case is obtained for ∼26 MeV seed protons, as seen in figure 4(c), which enter the HC2 with ∼35 MeV after acceleration in HC1. These protons are injected into the HC2 at ∼150 ps, slightly behind the EM pulse reaching the HC2 at 140 ps, and experience a small deceleration over the first few mm inside the HC2 before they penetrate into the accelerating positive field region as shown in figure 4(a1).

Figure 4(c) shows dynamics in energy gain vs seed energy for various τ, highlighting the accuracy in time of injection required to achieve an optimal energy gain in a multi-stage configuration. At the same time, figure 4(c) also indicates the flexibility of tuning optically the output energy in a given set of HCs. The majority of the temporal scan indicates substantial acceleration in HC2, though the energy gain varies due to the highly dynamic interaction between the protons and the electric fields within the DSHC targets. The maximum energy gain across the τ range was observed for $\tau = 180$ ps, although this produced a lower spectral peak than the case with $\tau = 140$ ps. In this experiment shown here, we chose to have a broadband seed beam into the second stage, and chose to select narrowband in the second coil. However, we can minimise transmission losses through appropriate coil designs, and any subsequent coil stages that could be added may not incur significant transmission losses if the coils are designed to collect the entire exit flux from the preceding stage, thus resulting in a significant proton flux even after multiple stages of acceleration. Future work aimed to explore the feasibility of operating the HC targets at high repetition will be crucial to envisage a pragmatic approach towards developing a compact beam delivery system for the aforementioned applications.

5. Conclusion

In conclusion, we have demonstrated successful deployment of HC targets in a double stage configuration, which is a promising first step towards building a miniature, modular, all-optical accelerator. Due to the short duration of the EM pulses driving the HCs, the experimental data highlights the requirement for precise timing on the ps-scale for an optimum performance, which offers tunability of output energy. A

modular approach not only provides better control over beam parameters, but also may offer an alternative route to reaching proton energies of therapeutic relevance (i.e. above 60 MeV) by using multiple pulses at more moderate power, rather than a single laser pulse at PW power or above. The multi-stage approach also addresses the issue of desynchronisation in HC accelerators as highlighted in earlier works [13, 18], which hinders the continuous acceleration of a desired proton bunch to high energies. This data serves as a proof of principle work for further exploration on multi-PW, multi-beam systems which will become available in coming years [27–30].

Data availability statement

The data that support the findings of this study are available upon reasonable request from the authors.

Acknowledgments

The authors acknowledge funding from EPSRC [EP/P010059/1 and EP/K022415/1], and the IMPULSE project by the European Union Framework Program for Research and Innovation Horizon 2020 under grant agreement No 871161. Authors also acknowledge the support of the target fabrication and mechanical engineering staff of the Central Laser Facility, STFC, UK. Authors also acknowledge A Schiavi for the use of the particle tracing code *PTRACE*.

ORCID iDs

P Martin https://orcid.org/0000-0002-0928-7445
M Alanazi https://orcid.org/0000-0003-4944-5580
M Cerchez https://orcid.org/0000-0002-9294-8397
S Kar https://orcid.org/0000-0002-9406-3103

References

[1] Macchi A, Borghesi M and Passoni M 2013 Ion acceleration by superintense laser-plasma interaction *Rev. Mod. Phys.* **85** 751
[2] Wilks S C, Langdon A B, Cowan T E, Roth M, Singh M, Hatchett S, Key M H, Pennington D, MacKinnon A and Snavely R A 2001 Energetic proton generation in ultra-intense laser-solid interactions *Phys. Plasmas* **8** 2
[3] Kar S *et al* 2016 Guided post-acceleration of laser-driven ions by a miniature modular structure *Nat. Commun.* **7** 10792
[4] Kar S, Ahmed H, Nersisyan G, Brauckmann S, Hanton F, Giesecke A L, Naughton K, Willi O, Lewis C L S and Borghesi M 2016 Dynamic control of laser driven proton beams by exploiting self-generated, ultrashort electromagnetic pulses *Phys. Plasmas* **23** 055711
[5] Bulanov S, Esirkepov T, Khoroshkov V and Pegoraro F 2002 Oncological hadron therapy with laser ion accelerators *Phys. Lett.* A **299** 240
[6] Bayart E *et al* 2019 Fast dose fractionation using ultra-short laser accelerated proton pulses can increase cancer cell mortality, which relies on functional PARP1 protein *Sci. Rep.* **9** 10132
[7] Chaudhary P, Milluzzo G, Ahmed H, Odlozilik B, McMurray A, Prise K M and Borghesi M 2021 Radiobiology experiments with ultra-high dose rate laser-driven protons: methodology and state-of-the-art *Front. Phys.* **9** 624963
[8] Kroll F *et al* 2022 Tumour irradiation in mice with a laser-accelerated proton beam *Nat. Phys.* **18** 316–22
[9] Alejo A *et al* 2016 Numerical study of neutron beam divergence in a beam-fusion scenario employing laser driven ions *Nucl. Instrum. Methods Phys. Res.* A **829** 176
[10] Mirfayzi S *et al* 2017 Experimental demonstration of a compact epithermal neutron source based on a high power laser *Appl. Phys. Lett.* **111** 044101
Mirfayzi S *et al* 2020 A miniature thermal neutron source using high power lasers *Appl. Phys. Lett.* **116** 174102
[11] Zimmer M *et al* 2022 Demonstration of non-destructive and isotope-sensitive material analysis using a short-pulsed laser-driven epithermal neutron source *Nat. Commun.* **13** 1173
[12] Patel P K, Mackinnon A J, Key M H, Cowan T, Foord M, Allen M, Price D, Ruhl H, Springer P and Stephens R 2003 Isochoric heating of solid-density matter with an ultrafast proton beam *Phys. Rev. Lett.* **91** 12
[13] Ahmed H *et al* 2021 High energy implementation of coil-target scheme for guided re-acceleration of laser-driven protons *Sci. Rep.* **11** 699
[14] Bardon M *et al* 2020 Physics of chromatic focussing, post-acceleration and bunching of laser-driven proton beams in helical coil targets *Plasma Phys. Control. Fusion* **62** 125019
[15] Quinn K *et al* 2009 Laser-driven ultrafast field propagation on solid surfaces *Phys. Rev. Lett.* **102** 194801
[16] Tokita S, Sakabe S, Nagashima T, Hashida M and Inoue S 2015 Strong sub-terahertz surface waves generated on a metal wire by high-intensity laser pulse *Sci. Rep.* **5** 8268
[17] Ahmed H *et al* 2016 Investigations of ultrafast charge dynamics in laser-irradiated targets by a self probing technique employing laser driven protons *Nucl. Instrum. Methods Phys. Res.* A **829** 172
[18] Hadjisolomou P *et al* 2020 Dynamics of guided post-acceleration of protons in a laser-driven travelling-field accelerator *Plasma Phys. Control. Fusion* **62** 115023
[19] Hernandez-Gomez C *et al* 2007 An overview of the Target Area West short pulse upgrade *Central Laser Facility Annual Report (2007/2008)*
[20] Musgrave I *et al* 2013 Recent developments on the Vulcan high power laser facility *Proc. SPIE* **8780** 878003
[21] Nurnberg F *et al* 2009 Radiochromic film imaging spectroscopy of laser-accelerated proton beams *Rev. Sci. Instrum.* **80** 033301

[22] Kirby D, Green S, Fiorini F, Parker D, Romagnani L, Doria D, Kar S, Lewis C, Borghesi M and Palmans H 2011 Radiochromic film spectroscopy of laser accelerated proton beams using the FLUKA code and dosimetry traceable to primary standards *Laser Part. Beams* **29** 231
[23] Gafchromic 2022 Gafchromic dosimetry media type HD-V2 user guide (available at: www.gafchromic.com/documents/gafchromic-hdv2.pdf)
[24] Gafchromic 2022 Gafchromic dosimetry media type EBT-3 user guide (available at: www.gafchromic.com/documents/EBT3_Specifications.pdf)
[25] Ahmed H *et al* 2017 Efficient post-acceleration of protons in helical coil targets driven by sub-ps laser pulses *Sci. Rep.* **7** 10891
[26] Schiavi A 2003 Study of laser produced plasmas by x-ray and proton radiography *PhD Thesis* Imperial College London
[27] Extreme Light Infrastructure - Nuclear Physics 2020 (Available at: www.eli-np.ro/)
[28] Extreme Light Infrastructure - Beamlines 2022 (Available at: www.eli-beams.eu/)
[29] Apollon 2022 (Available at: https://apollonlaserfacility.cnrs.fr/en/laser-beams/)
[30] Gan Z *et al* 2021 The Shanghai superintense ultrafast laser facility (SULF) project *Progress in Ultrafast Laser Science XVI* (Cham: Springer) pp 199–217